Microstructured elastomeric surfaces with reversible adhesion and examples of their use in deterministic assembly by transfer printing

Seok Kim[a], Jian Wu[b,1], Andrew Carlson[a,1], Sung Hun Jin[a], Anton Kovalsky[a], Paul Glass[c], Zhuangjian Liu[d], Numair Ahmed[e], Steven L. Elgan[e], Weiqiu Chen[f], Placid M. Ferreira[e], Metin Sitti[g], Yonggang Huang[b,2], and John A. Rogers[a,2]

[a]Department of Materials Science and Engineering, Beckman Institute, and Seitz Materials Research Laboratory, University of Illinois at Urbana-Champaign, Urbana, IL 61801; [b]Department of Civil and Environmental Engineering and Department of Mechanical Engineering, Northwestern University, Evanston, IL 60208; [c]Department of Biomedical Engineering, Carnegie Mellon University, Pittsburgh, PA 15213; [d]Institute of High Performance Computing, Singapore 138632; [e]Department of Mechanical Science and Engineering, University of Illinois at Urbana-Champaign, Urbana, IL 61801; [f]Department of Engineering Mechanics, Zhejiang University, Hangzhou, Zhejiang, China 310027; and [g]Department of Mechanical Engineering, Carnegie Mellon University, Pittsburgh, PA 15213

Edited by George M. Whitesides, Harvard University, Cambridge, MA, and approved August 10, 2010 (received for review April 27, 2010)

Reversible control of adhesion is an important feature of many desired, existing, and potential systems, including climbing robots, medical tapes, and stamps for transfer printing. We present experimental and theoretical studies of pressure modulated adhesion between flat, stiff objects and elastomeric surfaces with sharp features of surface relief in optimized geometries. Here, the strength of nonspecific adhesion can be switched by more than three orders of magnitude, from strong to weak, in a reversible fashion. Implementing these concepts in advanced stamps for transfer printing enables versatile modes for deterministic assembly of solid materials in micro/nanostructured forms. Demonstrations in printed two- and three-dimensional collections of silicon platelets and membranes illustrate some capabilities. An unusual type of transistor that incorporates a printed gate electrode, an air gap dielectric, and an aligned array of single walled carbon nanotubes provides a device example.

biomimetic | dry adhesion | elastomeric stamp | flexible electronics | microelectromechanical systems

Modes of adhesion observed in insects and small animals such as geckos are repeatable, robust, and power efficient. In fact, certain features such as the ability to adhere to a wide variety of surfaces, to rapidly and reversibly change adhesion strength between strong and weak modes, and to self-clean contaminants significantly exceed those available in conventional pressure sensitive tapes or structural adhesives. Many of these creatures have micro and nanoscale structures with varying levels of complexity on foot or toe-pads (1). Some of these beneficial aspects can be reproduced in synthetic materials, to yield dry adhesives (2–4) that offer, for example, switchability in adhesion through changes in thermal and/or mechanical conditions (3, 4). Although most reports focus on fibrillar structures mimicking those found on the feet of gecko lizards, attachment mechanisms that emulate adhesion organs or pads of common insects might provide attractive alternatives. For example, when adhering to or releasing from a smooth surface, aphid adhesion organs (*pulvilli*) are everted by increased blood pressure or withdrawn by contraction of tibial muscles (5), respectively. This pressure driven mechanical sagging or retraction of the *pulvillus* enlarges or diminishes the contacting areas, in a reversible fashion that induces corresponding changes in adhesion strength. This and related biological strategies provide opportunities for controlled adhesion in engineered systems, with one area of possible utility in methods for deterministic assembly of micro/nanomaterials by transfer printing. Here we introduce an adhesive surface inspired by the aphid in which pressure induced sagging of a microstructured elastomeric surface provides extreme, reversible levels of switchability in nonspecific, generalized adhesion, with strong to weak adhesion ratios higher than 1,000. The designs, which we refer to as microtip surfaces, are robust, reusable, and can be easily cleaned with commercial pressure sensitive adhesives like Scotch™ tape. Experimental and theoretical studies provide insights into the basic mechanisms of adhesion. We exploit these ideas in advanced stamps for printing-based assembly of silicon nanomembranes and platelets on a variety of surfaces, in two- and three-dimensional layouts that would be difficult or impossible to accommodate using other methods. As a device example, we use printing to form an unusual type of carbon nanotube transistor that uses a nanoscale air gap as a gate dielectric.

The adhesives reported here have potential uses in many applications. Our principal motivation is for advanced capabilities in the manipulation of stiff, solid micro/nano-objects via their selective transfer from one substrate (i.e., donor substrate) to another substrate (i.e., receiver substrate) using soft, elastomeric stamps. This transfer printing process (6–9) enables massively parallel assembly of diverse materials (i.e., Si, GaN, GaAs, mica, graphene, silica, and others) in various structural forms (i.e., wires, membranes, plates, with dimensions from a few nanometers to macroscopic scales), with throughputs that correspond to millions of objects per hour. A rapidly growing number of applications in micro and nanotechnology benefit from or are enabled by this type of approach (6–8). Transfer yields depend critically on the ability to switch from strong to weak adhesion between retrieval (i.e., "inking") and delivery (i.e., "printing"), respectively, and to maximize the versatility, control must be accomplished without specialized surface chemistries or adhesives. Kinetic approaches that exploit viscoelastic effects in the stamps (9) are useful, but the low contrast in adhesion switching (i.e., ~3) limits their broad utility. The experimental results and associated theoretical models presented here provide alternative design strategies, with significantly enhanced capabilities for printing-based assembly, and the potential for other areas of use.

Results

Fig. S1*A* illustrates a representative elastomeric microtip surface, with key dimensions labeled. The geometry consists of four

Author contributions: S.K., P.M.F., M.S., Y.H., and J.A.R. designed research; S.K., J.W., A.C., S.H.J., A.K., P.G., N.A., S.L.E., and W.C. performed research; S.K., J.W., A.C., S.H.J., Z.L., P.M.F., M.S., Y.H., and J.A.R. analyzed data; and S.K., J.W., A.C., S.H.J., P.M.F., M.S., Y.H., and J.A.R. wrote the paper.

The authors declare no conflict of interest.

This article is a PNAS Direct Submission.

[1]J.W. and A.C. contributed equally to this work.

[2]To whom correspondence may be addressed. E-mail: jrogers@uiuc.edu and y-huang@northwestern.edu.

This article contains supporting information online at www.pnas.org/lookup/suppl/doi:10.1073/pnas.1005828107/-/DCSupplemental.

features of pyramidal relief on the surfaces of square posts in a square array placed on a ~1 mm thick backing layer of the same material, configured to allow collapse of the regions of each post between the pyramids when subjected to sufficient applied force. This design enables extremely high levels of switching in adhesion, with a physics that involves a complex interaction between the pressure-controlled contact area and aspects of soft adhesion inherent in the viscoelastic nature of the elastomer, as revealed through systematic studies presented next. We begin with a qualitative description of the process for use in transfer printing (Fig. 1), and then outline some aspects of design, supported by quantitative measurements and theory. During retrieval, downward force mechanically collapses the regions between the microtips, thereby maximizing the contact area and, as a result, the strength of generalized adhesion, typically dominated by van der Waals interactions (10), between the object to be transferred (green platelet in Fig. 1) and the stamp. For sufficiently low strengths of adhesion to the donor substrate, retracting at high speeds retrieves the platelet, in a way that maximizes adhesion to the stamp through viscoelastic effects. Immediately after retraction, elastic restoring forces bring the relief back to its original geometry, leaving contact only at the sharp points of the microtips. To affect printing, the stamp, inked in this manner, presses against a receiver surface such that the platelet comes into complete contact on its bottom surface, but the relief on the stamp does not collapse. Slow retraction minimizes the adhesion strength associated with viscoelastic effects, thereby facilitating release and completing the transfer printing assembly process.

A custom measurement setup provides the ability to quantify the adhesion (Fig. S2*A*). The system consists of motorized *x*, *y* stages and a manual tilting stage (Newport, UTR46) that supports a precision load cell (Transducer Techniques, GSO-10). Microtip surfaces, similar to the one illustrated in Fig. 1 and Fig. S1*A* are mounted on an independent vertical stage (Aerotech, PRO165) that allows contact with a target substrate (i.e., silicon wafer for the results presented here) at controlled speeds and forces. For the work presented here, we formed these surfaces with the elastomer poly(dimethylsiloxane) (PDMS), using casting and curing procedures of soft lithography with appropriate templates (Fig. S1*B*). PDMS is a transparent elastomer with well known, attractive properties for this application, such as linear elastic response to elongations of 100% or more, high physical toughness, and excellent fatigue characteristics. Fig. 2 *A–D* provide SEM images of a structure in the design of Fig. 1 and Fig. S1*A*, without and with an adhering silicon platelet and a schematic illustration for the latter case. Fig. 2 *E*, *F* show an advanced configuration that involves the addition of a large microtip in the center, for purposes described subsequently. Fig. 3 *A*, *B* present typical force-time plots for a single post having the four-tipped design, with distance scales indicated on the top axes, collected at an approach speed of 5 μm/s, terminated at a specified load for 5 s, and then retracted at 1 mm/s. The maximum tensile force during retraction defines the strength of adhesion (i.e., pull-off). Fig. 3*A* shows data for a representative case of full mechanical collapse under a preload of 1 mN, with a retraction speed of 1 mm/s. Two slopes are evident in the approaching curve (red line), indicating an increase in stiffness when the region between the microtips collapses and contacts the substrate. The slope in the first region defines an effective spring constant associated with compression of the microtips, with a minor contribution from deformation of the post. The second region includes the elasticity of the post itself, and its elastomeric support. The sharp, negative feature in the curve collected during retraction (blue line) corresponds to rapid release from the contacting surface; its magnitude defines the adhesion force (i.e., pull-off). Fig. 3*B* summarizes the corresponding case without collapse, at 0.2 mN preload and 1 mm/s retraction. Here, the adhesion force is too small to measure with the load cell. Images collected with an inverted optical microscope and an SEM (Fig. 2 and Fig. S3*A*) suggest effective contact areas in the collapsed and uncollapsed states that correspond to ~80% and ~0.07% of the projected area of the post and the microtips, respectively. The ratio of these areas suggests an expected difference in adhesion of more than 1,000 times. This value, however, underestimates the actual difference that can be achieved because it ignores viscoelastic effects, as observed clearly in the data of Fig. 3*C*. In particular, with preloads sufficient to induce mechanical collapse (i.e., 1.5 mN and 3 mN), the adhesion force depends strongly on retraction speed. This functional dependence, which is evident also in data for the corresponding flat surfaces (Fig. 3*D*), arises from the viscoelastic nature of the PDMS, as reported previously (9). We did not observe any significant changes in these adhesion behaviors even on repeated cycling tests (Fig. S2*B*).

These combined geometric and material effects offer exceptionally high levels of switching in adhesion, for unmatched capabilities in transfer printing, without the need for surface chemistries or separate adhesives to guide transfer. For purposes of demonstration, we use platelets of silicon (100 × 100 μm; thicknesses of 260 nm or 3 μm) fabricated by removing the buried oxide layer from a silicon-on-insulator (SOI) wafer, as illustrated in Fig. S1*C*. Fig. 4*A* shows such platelets printed onto an array of islands (7 × 7 μm squares, separated by 13 μm with square packing arrangement). The ability to transfer at high yields without adhesives, particularly on structured surfaces where contact areas with the receiver are much smaller than the areas of the platelets themselves, clearly illustrates the utility of the microtip design; these capabilities are unavailable to methods that just use viscoelastic effects for control (9). As a more challenging example, Fig. 4*B* shows results of printing onto the rough surface of a film of ultrananocrystalline diamond (2 μm thick, rms roughness >70 nm with sharp facet edges; see inset), where we estimate the contact area to be less than 1% of the platelet area. Stamps

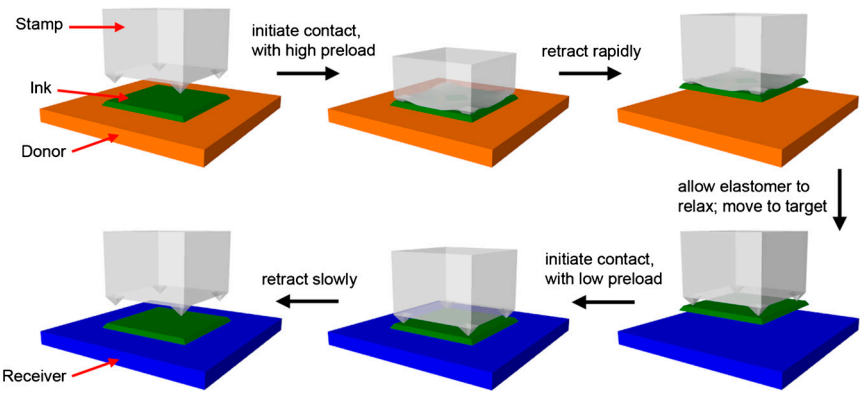

Fig. 1. Implementation of elastomeric, microtip adhesive surface in a stamp for deterministic assembly by transfer printing.

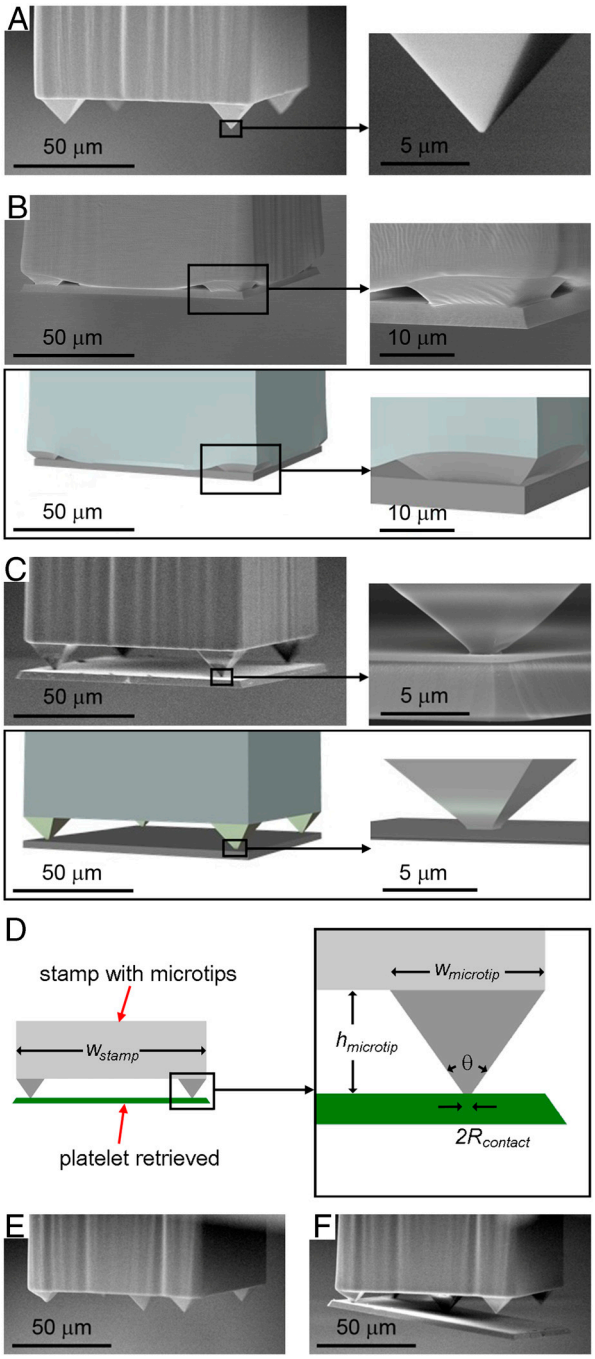

Fig. 2. SEM and FEM images of representative elastomeric stamps in microtip designs, with and without silicon platelets (3 μm thick; 100 × 100 μm) on their surfaces. (*A–C*) Four-tipped layout. The right frames provide magnified views of one of the microtips and the bottom frames provide corresponding images of the results of finite element modeling (*B*, *C*). (*D*) Schematic illustration for notation of the stamp dimension. (*E*, *F*) Five-tipped layout. In this design, the silicon platelet remains in contact only with the largest, central microtip in the final stages of the transfer printing process.

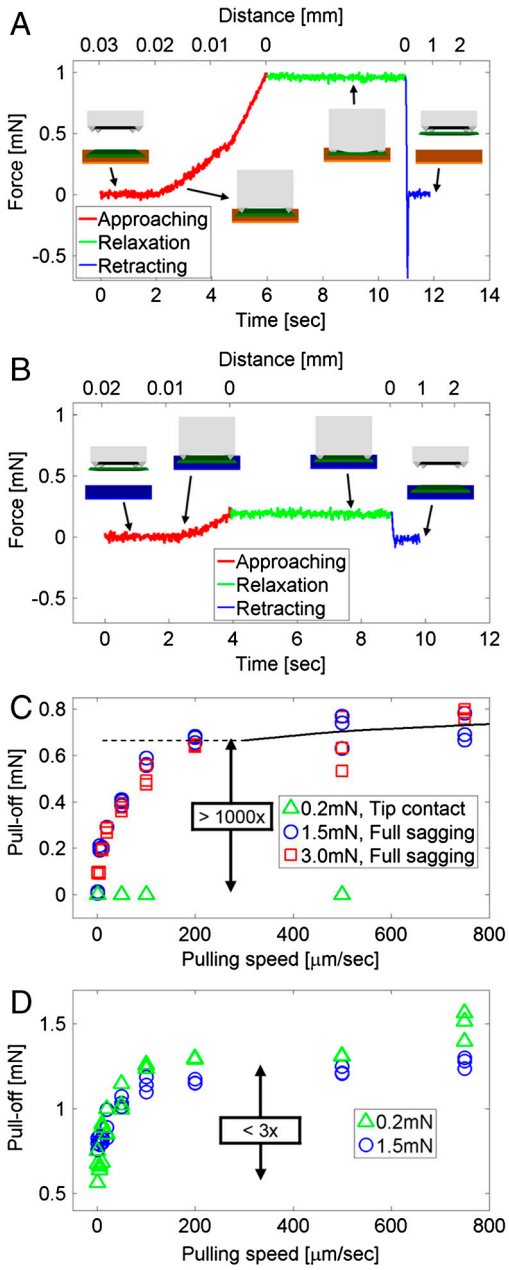

Fig. 3. Typical force-time (bottom axis) and force-distance (top axis) curves associated with contact of a microtip surface with the flat surface of a silicon wafer (*A*, *B*). The inset illustrations correspond to the steps of retrieval (*A*) and delivery (*B*) for use of such a surface in a transfer printing mode. Plots of force required to remove a microtip surface (*C*) and a corresponding flat surface (*D*) from the silicon, as a function of retraction speed for three different preload cases, simulating the steps of retrieval (0.2 mN) and delivery (1.5, 3 mN) in a printing process. Modeling results for the microtip surface are indicated as a black line (*C*).

with five microtips (Fig. 2 *E*, *F* and Fig. S3*B*) were needed for successful printing of 260 nm thick platelets, where adhesion in the printing mode can be quite small, due to contact only at the single, central microtip in the final stages of release. Freely suspended geometries are also possible. Fig. 4 *C*,*D* show printed platelets (3 μm and 260 nm thick) that span gaps between pairs of silicon bars on receiver substrates. The high yield and versatility of this process also enable the formation of complex, three-dimensional assemblies. Fig. 4 *E*, *F* provide images of multilayer configurations of 3 μm thick silicon platelets in single and multiple stacks with translational and rotational increments. These examples demonstrate a construction capability for three-dimensional micro/nanostructures that approaches those of macroscale fabrication methods based on assembly of building blocks, e.g., *LEGO*® with silicon.

Similar microtip designs can be exploited in the fabrication of active devices for applications in areas ranging from photonics and metamaterials to photovoltaics and electronics. To demonstrate an example, we built an unusual class of transistor that

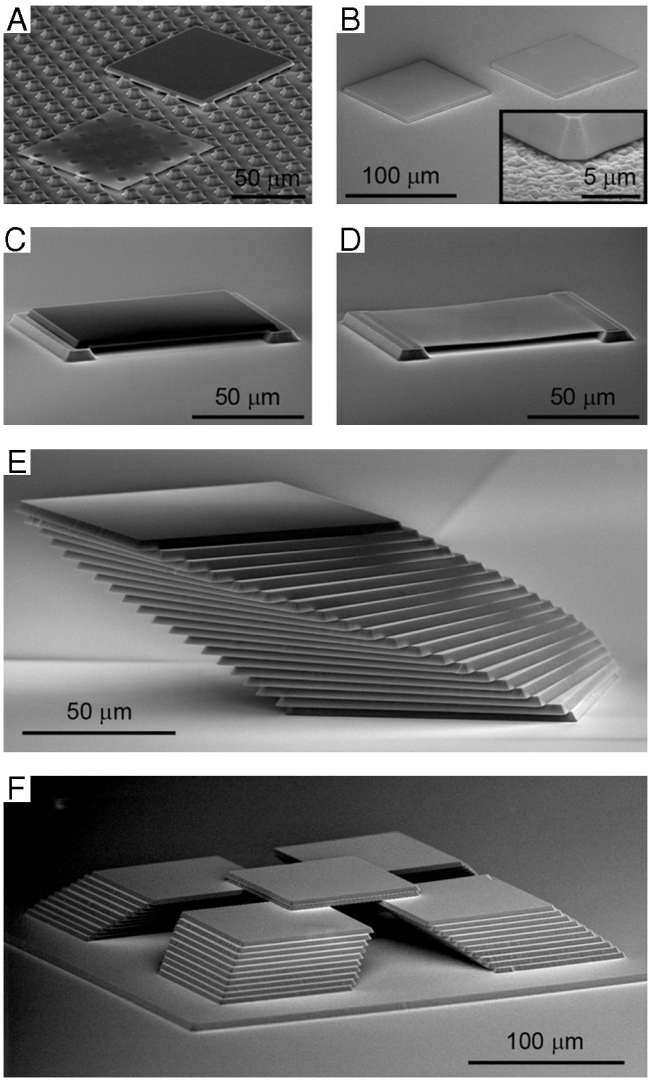

Fig. 4. SEM images of representative printing results with thick (3 μm) and thin (260 nm) silicon platelets (100 × 100 μm squares) on different surfaces and in free standing and multilayer stacked geometries. (*A*) Image of platelets printed on an array of square islands. (*B*) Image of 3 μm thick silicon platelets printed on the rough surface of a film of ultrananocrystalline diamond on a silicon wafer. Images of 3 μm (*C*) and 260 nm (*D*) thick silicon platelets printed onto two silicon bars, to yield freely suspended structures. Images of multilayer configurations of 3 μm thick silicon platelets in a single stack with small incremental rotations and translations (*E*) and four similar stacks, capped with a pair of platelets in the center (*F*), both on flat silicon wafer substrates.

combines a printed gate electrode, an air gap dielectric, and a parallel array of single walled carbon nanotubes. Fabrication steps and characterization details are described in *SI Text*.

Discussion

The pyramid geometry a microtip has certain practical advantages: (*i*) it is easy to fabricate in a well controlled, lithographic manner using techniques of anisotropic etching in silicon and (*ii*) the radius of curvature of the tip can be extremely small, and it is decoupled from the overall height of the relief feature (i.e., the microtip). The underlying mechanics principles can be used with other shapes.

Data analysis guided by theoretical mechanics modeling reveals the underlying physics of adhesion in surfaces of the type described previously, and identifies the key parameters for optimization. We first consider the strength of the low adhesion state, where the adhesion energy per unit area in the limit of zero peel rate multiplied by the area of contact at the ends of the microtips is important. Fig. 2 *A*, *C* show a representative case, where the stamp, made of PDMS, incorporates anisotropically etched pits in silicon (100), to yield microtips with radii of curvature, R_{microtip}, less than ~100 nm (Fig. S1*B*). Contact with the silicon causes the microtips to deform, to maintain equilibrium between attraction from surface adhesion and elastic repulsion. These deformations lead to contact areas that are considerably larger than those that might be inferred based only on the geometry of the stamp. Classical models of contact mechanics (11) can be adapted to give analytically the contact radius R_{contact} (Fig. 2*D*) (see *SI Text* for details)

$$\frac{R_{\text{contact}}}{\gamma/\tilde{E}} = s\left(\frac{R_{\text{microtip}}}{\gamma/\tilde{E}}, \theta\right), \qquad [1]$$

where s is a nondimensional function of the microtip cone angle θ (Fig. 2*D*) and R_{microtip} (Fig. S1*A*) is given in *SI Text*. Finite element analysis yields similar results (see Fig. 2*C* and the *SI Text*). The value of R_{contact} scales linearly with the work of adhesion γ between the PDMS and the contacting surface, and inversely with the plane-strain modulus $\tilde{E} = E/(1-\nu^2)$ of PDMS (E–Young's modulus, $\nu \approx 0.5$–Poisson's ratio). Analysis shows that R_{contact} decreases with R_{microtip}, but reaches an asymptotic value for $R_{\text{microtip}} \to 0$ (Fig. S5*A*) given by

$$R_{\text{contact}}^{\text{min}} = \frac{32\gamma}{\pi\tilde{E}}\tan^2\frac{\theta}{2}. \qquad [2]$$

We note that our analytical models assume symmetric deformations, without any bending or buckling. The SEM and finite element method (FEM) results of Fig. 2 support the validity of this assumption.

For the case of a PDMS stamp and a silicon surface, where E = 1.8 MPa (12) and $\gamma = 155$ mJ/m^2, (13, 14), R_{contact} is approximately the same as $R_{\text{contact}}^{\text{min}}$ when R_{microtip} is less than ~100 nm (Fig. S1*B*). When $\theta = 90°$ between two opposite edges of pyramid ($w_{\text{microtip}} = \sqrt{2}h_{\text{microtip}}$ in experiments, Fig. S1*A*), $R_{\text{contact}}^{\text{min}}$ is ~680 nm, comparable to 750 nm evident from Fig. 2*C*, and 732 nm given by the finite element method (Fig. 2*C* and *SI Text*). The conclusion, then, is that existing methods for producing elastomer surfaces in a material like PDMS can already achieve values of R_{microtip} well below the value needed to realize minimal contact area. Advanced microtip layouts can, however, reduce the contact area below that provided by the four tip design. Fig. 2 *E*, *F* show examples of such reduced contact area schemes. In these designs, during release separation occurs initially at the smaller corner microtips leaving the final central microtip in contact with the platelet, thereby reducing the contact area immediately before release to the minimum possible value immediately before release (Fig. S3*B*), (four times lower than that associated with Fig. 2*C*). Further reductions might be possible by increasing E, with other silicones, or decreasing γ, with related elastomers such as perfluoropolyethers, or decreasing the microtip cone angle θ.

The heights of the microtips and their nearest neighbor separations represent other critical parameters. The designs must enable unstable collapse, with near full area contact in the compressed state. For a given separation, there exists a minimum height of the microtip, h_{min}, below which the elastic restoring force is too small to bring the relief back to its original geometry after pressure induced collapse. This minimum height can be determined by equating the strain energy in the compressed PDMS and microtips to the adhesion energy between the contacting surfaces, which gives (see *SI Text* for details), for the four tip design,

$$h_{\min} = \sqrt{\frac{w_{\text{stamp}}\gamma}{\bar{E}}\left[3.04\ln\left(\frac{w_{\text{stamp}}\bar{E}}{\gamma\tan^2\frac{\theta}{2}}\right) - 11.5\right]}, \quad [3]$$

where w_{stamp} is the width of the post of the stamp. For $w_{\text{stamp}} = 100$ μm ($E = 1.8$ MPa, $\gamma = 155$ mJ/m^2, and $\theta = 90°$), the above expression gives $h_{\min} = 8.44$ μm, which agrees well with the minimum height of ~8.5 μm observed systematically in experiments (see Fig. S5*B* and *SI Text* for details). There also exists a maximum height, $h_{\max}$, above which the elastic restoring force associated with compression of the microtips is so large that the stamp rapidly delaminates from the platelet after the pull-off force is applied, thereby preventing large contact areas for efficient removal of an object (e.g., platelet, as illustrated in Fig. 1) from a donor substrate. The value of $h_{\max}$ can be determined analytically by equating the energy release rate to the work of adhesion between the PDMS stamp and the silicon platelet. The result is (see *SI Text* for details)

$$h_{\max} = w_{\text{stamp}} f\left(\frac{P}{w_{\text{stamp}}^2\bar{E}}, \frac{w_{\text{microtip}}}{w_{\text{stamp}}}, \frac{\gamma}{w_{\text{stamp}}\bar{E}}\right), \quad [4]$$

where f is a nondimensional function of the applied force P, the microtip width (w_{microtip}, Fig. S1*A*), and the work of adhesion γ. For the full expression, see the *SI Text*. For an applied force of 1 mN and $w_{\text{microtip}} = \sqrt{2}h_{\text{microtip}}$ (other material and geometry parameters the same as before), the maximum height is $h_{\max} = 13.3$ μm, which agrees reasonably well with the maximum height of ~12.7 μm from experiments (see Fig. S5 *C*,*D* and *SI Text* for details). These minimum and maximum values elucidate criteria that define three possible energy states of the stamp and the platelet: (*i*) platelet retrieval with relief collapsed, (*ii*) platelet retrieval with relief delaminated, (*iii*) failure in platelet retrieval. The microtip sizes were optimized to obtain the second state for representative preload forces (>1 mN) and retrieval velocities (>200 μm/s). Experiments with different microtips showed that when h is ~20% smaller or larger than this optimal value, states (*i*) (platelet retrieval with relief collapsed) or (*iii*) (failure in platelet retrieval) with the same preloads and velocities could be achieved, respectively.

The rate dependence observed in the microtip structures is identical, to within experimental uncertainties, to that in flat post stamps. The latter effects were explored previously by us, in the case of transfer printing (9), and by many others in the more general context of adhesion between viscoelastic and nonviscoelastic materials (10, 13, 15).

For operation in the retrieval mode, the stamp must be retracted sufficiently quickly that the fracture of the interface between the platelets and their donor substrate occurs before the viscoelastic fracture of the stamp/platelet interface. During fast retraction the compressed microtips do not have time to relax back to their original shapes; their heights remain small and the overall contact area remains high, such that the energy release rate is lower than the work of adhesion. An analytical viscoelastic model, with creep compliance data for PDMS from the literature (16), gives a relaxation time of 0.052 s (for pulling speed 460 μm/s), at which the collapsed stamp starts to debond from the substrate (see *SI Text*). For fast retraction (pulling speed >200 μm/s), this time scale is roughly consistent with experimental observation because the time for complete separation of the stamp/substrate interface is about the same as the time for initial debonding. Additionally, this viscoelastic analysis predicts a pull-off force that is in quantitative agreement with the experiments at pulling speeds >200 μm/s, as shown in Fig. 3*C*. For pulling speeds <200 μm/s, the analysis gives a larger pull-off force than the experiments because the debonding may gradually propagate along the stamp/substrate interface due to slow retraction, but the model does not account for crack propagation along the interface. Improved analysis and comparison to experiment will require accurate measurements of creep compliance in our PDMS and direct visualization of the interface using high speed imaging techniques. These topics are the focus of future work.

The force-distance curves and other behaviors of Fig. 3 can also be captured by mechanics modeling. For the case of Fig. 3*A*, modeling predicts two slopes, as observed in experiment: k_{microtip} when contact occurs only at the microtips, and k_{post} for contact at both the microtips and the intervening regions. In particular, analysis yields (see *SI Text*)

$$\frac{1}{k_{\text{microtip}}} = \frac{1}{k_{\text{post}}} + \frac{1}{Ew_{\text{microtip}}}\left[\frac{3h_{\text{microtip}}}{4w_{\text{microtip}}} + \frac{1}{\pi}\left(\frac{w_{\text{microtip}}}{w_{\text{stamp}}} - 2\frac{w_{\text{microtip}}^3}{w_{\text{stamp}}^3}\right)\ln\left(\frac{w_{\text{stamp}}^2}{2w_{\text{microtip}}^2} - 1\right)\right]. \quad [5]$$

For $k_{\text{microtip}} = 30$ N/m and $k_{\text{post}} = 90$ N/m extracted from Fig. 3*A*, and $h_{\text{microtip}} = 10.6$ μm and width $w_{\text{microtip}} = \sqrt{2}h_{\text{microtip}} = 15$ μm from experiments, the left- and right-hand sides of Eq. **5** give 0.033 m/N and 0.036 m/N, respectively. This excellent level of agreement validates the modeling, and its further use in examining the differences between Fig. 3 *C* and *D* to gain insights into the adhesion mechanics. In the collapsed state, the microtips provide forces that add to the externally applied force needed to cause delamination. This effect can be explored through calculation. In particular, the mechanics models described previously yield analytical forms for the restoring force, F, associated with the compressed microtips. The result takes the form (see *SI Text* for details)

$$F = w_{\text{stamp}}^2\bar{E}g\left(\frac{P}{w_{\text{stamp}}^2\bar{E}}, \frac{w_{\text{microtip}}}{w_{\text{stamp}}}, \frac{h_{\text{microtip}}}{w_{\text{stamp}}}\right), \quad [6]$$

where g is a nondimensional function of the applied force P, microtip width w_{microtip}, and height h_{microtip}, and is given in the *SI Text*. This force, as shown in Fig. S6*A*, is the same as the preload when only microtips contact the platelet. The sudden increase in the restoring force corresponds to the collapse of post between microtips. This force then increases linearly with the preload (post contact in Fig. S6*A*), but with reduced slope due the elasticity of the post. This dependence is followed by a nonlinear increase, at a reduced rate because the contact area also increases (zipping of interface in Fig. S6*A*). For an applied force of 1.5 mN, the total restoring force is 0.63 mN for the collective effect of four microtips with height $h_{\text{microtip}} = 10.6$ μm and width $w_{\text{microtip}} = \sqrt{2}h_{\text{microtip}} = 15$ μm (other material and geometry parameters are the same as above). Note that this restoring force is larger than the preload 0.39 mN needed to cause collapse of the regions between the microtips (i.e., position in the red curve of Fig. 3*A* that occurs at the point where the linear slope changes) because the microtips continue to be compressed after the intervening regions collapse (see Fig. S6*A*). Fig. S6*B* presents a master plot obtained by shifting the data of Fig. 3*D* downward along the y-axis by an amount equal to the total restoring force evaluated by modeling, and the plotting results together with the data of Fig. 3*C*. The overlap of the resulting curves, to within experimental uncertainty, supports the modeling and the associated interpretation of the underlying physics.

Conclusion

This paper reports a unique adhesive surface for deterministic assembly of solid micro/nanoscale parts into two- and three-dimensional configurations, and some theoretical foundation for understanding key design parameters. The work provides experimental data and theoretical models on pressure induced switching in adhesion strength in these systems. Theoretically guided

design optimization yields high levels of control, with more than three orders of magnitude difference between the forces measured in strong and weak adhesive states. These characteristics enable transfer printing reliably and repeatedly with very high yield (almost 100%) in new modes, with important consequences for applications. Future opportunities include exploring other uses, and pursuing strategies for increasing the adhesion over the corresponding flat surface using vacuum effects or notched features on the sidewalls of the posts. These and other structural designs can be further enhanced through the introduction of new materials, using guidance from mechanical models similar to those presented here.

Materials and Methods

Fabrication of Elastomeric Surfaces with Microtips. The fabrication (Fig. S1*B*) involved casting and curing the elastomer PDMS (Sylgard 184, Dow Corning; 5:1 mixture of base to curing agent) against a Si (100) wafer (Addison Engineering) with a pattern of photodefined epoxy (SU-8 50; MicroChem Corp.; 100 μm thick) and an array of pyramidal pits (15 × 15 μm squares, 10.6 μm deep, separated by 70 μm with square packing arrangement) formed by anisotropic etching with KOH through a photolithographically patterned hard mask of SiN (100 nm thick, formed using plasma enhanced chemical vapor deposition, PECVD, PlasmaTherm). The epoxy layer provided square openings (100 × 100 μm) with corners aligned to sets of pits. Casting the prepolymer to PDMS (base oligomer and crosslinking agent) against the functionalized (trichlorosilane, United Chemical Technology) surface of this wafer, thermally curing the PDMS (70 °C for >1 h) and then peeling it back yielded the desired elastomeric surfaces with microtips.

Fabrication of Silicon Platelets for Printing. The printed structures consisted, in all cases, of flat plates of silicon (100) derived from SOI wafers (Shin-Etsu Chemical Co., Ltd. and Soitec), with thicknesses of 3 μm or 260 nm. These plates were defined by patterning a layer of photoresist (AZ5214, 1.5 μm thick) in a square geometry (100 × 100 μm, square packing arrangement, 300 μm separation) and then etching the exposed top Si by SF_6 reactive ion etching (PlasmaTherm). Next, wet etching with concentrated hydrofluoric acid, HF, through a mask of photoresist removed the buried oxide everywhere except for 110 × 110 μm squares cocentered with the squares of silicon. A final pattern of photoresist (AZ5214) defined mechanical anchor features (15 × 45 μm rectangles, 1.5 μm thick) to tether the silicon squares to the underlying wafer at each of their four corners. Undercut etching of the remaining oxide with HF completed the process. Fig. S1*C* summarizes the steps.

Transfer Printing. Precision translation and rotational stages controlled the positions of the stamps during the various steps in printing, as illustrated in Fig. 1. After each complete sequence of printing, the structures were annealed at 200–900 °C depending of receiver substrates in air for 3 min (TMC Services, Inc., Micristar Model 828) to eliminate residual photoresist and to increase the strength of adhesion.

ACKNOWLEDGMENTS. We thank T. Banks for help with processing. The work was supported by National Security Science and Engineering Faculty Fellowship (NSSEFF) and the Department of Energy (DEFG02-91ER45439). The printing and adhesion components used funding from a Multi-Univeristy Research Initiative (MURI) program and the National Science Foundation (DMI-0328162).

1. Arzt E, Gorb S, Spolenak R (2003) From micro to nano contacts in biological attachment devices. *Proc Natl Acad Sci USA* 100:10603–10606.
2. Geim AK, et al. (2003) Microfabricated adhesive mimicking gecko foot-hair. *Nat Mater* 2:461–463.
3. Murphy MP, Aksak B, Sitti M (2009) Gecko-inspired directional and controllable adhesion. *Small* 5:170–175.
4. Kim S, Sitti M, Xie T, Xiao X (2009) Reversible dry micro-fibrillar adhesives with thermally controllable adhesion. *Soft Matter* 5:3689–3693.
5. Lees AD, Hardie J (1988) The organs of adhesion in the aphid megoura viciae. *J Exp Biol* 136:209–228.
6. Kim DH, et al. (2008) Stretchable and foldable silicon integrated circuits. *Science* 320:507–511.
7. Fan Z, Ho JC, Jacobson JA, Razavi H, Javey A (2008) Large scale, heterogeneous integration of nanowire arrays for image sensor circuitry. *Proc Natl Acad Sci USA* 105:11066–11070.
8. Yu J, Bulović V (2007) Micropatterning metal electrode of organic light emitting devices using rapid polydimethylsiloxane lift-off. *Appl Phys Lett* 91:043102-1–043102-3.
9. Meitl MA, et al. (2006) Transfer printing by kinetic control of adhesion to an elastomeric stamp. *Nat Mater* 5:33–38.
10. Feng X, et al. (2007) Competing fracture in kinetically controlled transfer printing. *Langmuir* 23:12555–12560.
11. Maugis D (1995) Extension of the Johnson-Kendall-Roberts Theory of the elastic contact of spheres to large contact radii. *Langmuir* 11:679–682.
12. Kim DH, et al. (2009) Optimized structural designs for stretchable silicon integrated circuits. *Small* 5:2841–2847.
13. Chaudhury MK, Whitesides GM (1991) Direct measurement of interfacial interactions between semispherical lenses and flat sheets of poly(dimethylsiloxane) and their chemical derivatives. *Langmuir* 7:1013–1025.
14. Huang Y, et al. (2005) Stamp collapse in soft lithography. *Langmuir* 21:8058–8068.
15. Gent AN (1996) Adhesion and strength of viscoelastic solids. Is there a relationship between adhesion and bulk properties? *Langmuir* 12:4492–4496.
16. Xu Z, Kim K, Zou Q, Shrotriya P (2008) Broadband measurement of rate-dependent viscoelasticity at nanoscale using scanning probe microscope: Poly(dimethylsiloxane) example. *Appl Phys Lett* 93:133103-1–133103-3.

Supporting Information

Kim et al. 10.1073/pnas.1005828107

SI Text

Device Assembly Example. Fabricated microtip stamps using the design schemes illustrated in Fig. S1*A* exhibited large adhesion differences when characterized via systematic tests using the setup described in Fig. S2*A*. This difference is due primarily to the large contact area reduction between the adhesion "on" and "off" states (Fig. S3*A*). In addition, to demonstrate a device assembly example, we built an unusual class of transistor that combines a printed gate electrode, an air gap dielectric, and a parallel array of single walled carbon nanotubes. Fig. S4*A* shows such a device, with a 100 nm thick air gap dielectric and a gate electrode that consists of a heavily doped ($\rho = 0.0014\ \Omega$cm) silicon platelet (3 μm thick; 100×100 μm), delivered to the device structure by printing. Strategically located patterns of thin metal films provide support structures at the corners of the platelet to define its physical separation from the nanotubes (i.e., the thickness of the air gap dielectric). After growing aligned single walled carbon nanotubes (SWNTs) by chemical vapor deposition (CVD), source and drain electrodes were defined by electron-beam evaporation with 1 nm thick titanium, Ti, and 49 nm thick palladium, Pd, followed by consecutive lift off process in acetone. A peripheral area of SWNT was removed with oxygen reactive ion etching to yield electrically isolated devices. An air gap spacer with 100 nm thick gold was made by electron-beam evaporation and lift off process. A heavily doped ($\rho = 0.0014\ \Omega$cm) silicon platelet was transfer printed on a patterned poly(dimethylsiloxane) (PDMS) surface and then the residue of photoresist anchors was removed with acetone. Finally, the cleaned platelet was transfer printed from the PDMS surface to the air gap spacer and annealing process was performed on a hot plate at 200 °C for 30 min in ambient argon.

The variation in source/drain current (I_{DS}) as a function of gate voltage (V_{GS}) at a source/drain bias (V_{DS}) of −0.05 V for a representative device with channel length and width of 5 μm and 30 μm, respectively, (Fig. S4*B*) appears in Fig. S4*C*. Gate leakage currents less than 10 picoamps, pA, were observed at V_{GS} up to 7 V, where the field strength is somewhat larger than 2 megavolts per centimeter, MV/cm. Increased currents occur for higher voltages, somewhat lower than those expected based on air breakdown according to Pashen's law (1). Accurate models of the capacitance coupling (2) of the gate to the array of tubes (densities of ∼0.5 tubes/μm) can be used together with the measured properties in Fig. S4*C* to estimate the mobility; the result is ∼1,500 cm^2/Vsec, comparable to values reported for related devices with conventional layouts (3). We envision that the type of device presented here could be useful in applications, such as sensing in gases or liquids (4), where both gate modulation and physical access to the nanotubes are required.

Contact Radius at Zero Preload. The shape of microtips can be represented by a spherical portion near the tip and a conical portion in the cylindrical coordinates (r, z),

$$z = f(r) = \begin{cases} R_{\text{microtip}} - \sqrt{R_{\text{microtip}}^2 - r^2} & 0 \le r \le R_{\text{microtip}} \cos\frac{\theta}{2} \\ \frac{r}{\tan\frac{\theta}{2}} - R_{\text{microtip}}\left(\frac{1}{\sin\frac{\theta}{2}} - 1\right) & r > R_{\text{microtip}} \cos\frac{\theta}{2} \end{cases}. \quad \textbf{[S1]}$$

The contact mechanics model (5) relates the radius of contact R_{contact} to the above shape function $f(r)$, work of adhesion γ, and plane-strain modulus $\tilde{E}$ by

$$\frac{\tilde{E} R_{\text{contact}}}{2\pi}\left[\frac{\delta}{R_{\text{contact}}} - \int_0^{R_{\text{contact}}} \frac{f'(r)dr}{\sqrt{R_{\text{contact}}^2 - r^2}}\right]^2 = \gamma, \quad \textbf{[S2]}$$

where δ is related to the preload P by

$$P = 2\tilde{E}\int_0^{R_{\text{contact}}}\left[\delta - t\int_0^t \frac{f'(r)dr}{\sqrt{t^2 - r^2}}\right]dt. \quad \textbf{[S3]}$$

For zero preload $P = 0$, δ is given by

$$\delta = \frac{1}{R_{\text{contact}}}\int_0^{R_{\text{contact}}} \sqrt{R_{\text{contact}}^2 - r^2} f'(r)dr. \quad \textbf{[S4]}$$

The substitution of Eq. **S4** into Eq. **S2** gives the equation for R_{contact}

$$\frac{\tilde{E}}{2\pi R_{\text{contact}}^3}\left[\int_0^{R_{\text{contact}}} \frac{r^2 f'(r)dr}{\sqrt{R_{\text{contact}}^2 - r^2}}\right]^2 = \gamma. \quad \textbf{[S5]}$$

For the shape function in Eq. **S1**, Eq. **S5** gives the following equation for the ratio of radii $\eta = \frac{R_{\text{microtip}}}{R_{\text{contact}}}$,

$$\eta - \frac{\cos^{-1}(\eta\cos\frac{\theta}{2})}{\tan\frac{\theta}{2}} - \eta\frac{\sqrt{1-\eta^2\cos^2\frac{\theta}{2}}}{\sin\frac{\theta}{2}} + (1+\eta^2)\ln\frac{\sqrt{1-\eta^2\cos^2\frac{\theta}{2}} + \eta\sin\frac{\theta}{2}}{1+\eta} + 2\sqrt{\eta}\sqrt{\frac{2\pi\gamma}{\tilde{E}R_{\text{microtip}}}} = 0. \quad \textbf{[S6]}$$

Eq. **S6** gives the implicit expression in Eq. **1**. The contact radius, normalized by $\frac{\gamma}{\tilde{E}}$, is shown in Fig. S5*A*, and so is R_{contact} for material properties in the experiment. For $R_{\text{microtip}} \to 0$, it gives analytically the asymptote in Eq. **2**.

Eq. **S6** holds only when the contact between the microtips and platelet has reached the conical portion. Eq. **S6** requires small microtip radius of curvature,

$$\frac{\tilde{E}R_{\text{microtip}}}{\gamma} \le \frac{8\pi\cos^3\frac{\theta}{2}}{\left[(1+\cos^2\frac{\theta}{2})\ln(\tan\frac{\theta}{4}) + \cos\frac{\theta}{2}\right]^2}. \quad \textbf{[S7]}$$

For microtip radius of curvature exceeding this critical value, the contact between the microtips and platelet remains in the spherical portion, and the corresponding contact radius has been obtained analytically (5). The conical and spherical contacts are also clearly shown in Fig. S5*A*.

Finite Element Analysis of Contact Radius. The contact radii in Eqs. **1** and **2** are derived from classical models of contact mechanics (5), originally developed for the case of a rigid indenter in contact with a soft material. Similar models can be applied to soft indenters in contact with hard materials. For example, Lim and Chaudhri (6) measured the indentation load-displacement curve for a conical indenter of soft rubber in contact with a hard, soda-lime glass. The Young's moduli of rubber (2.45 MPa) and glass (70 GPa) are comparable to those of PDMS (1.8 MPa) and silicon (130 GPa), respectively, reported in main text. The conical indenter, which had the cone angle 60 degree, maximum radius 5 mm,

and round tip radius 0.23 mm, respectively, was used in Lim and Chaudhri's experiments (6).

We studied this axisymmetric indentation problem using the finite element method (FEM), which accounts for the geometric nonlinearity (large change of indenter shape) during indentation. The Poisson's ratio of indenter was 0.4999999 in FEM. We used axisymmetric elements for the rubber indenter, including the detailed geometry of the indenter tip. The element size was ~0.0345 mm, which is 7 times smaller than the indenter tip radius, and 150 times smaller than the maximum indenter radius. Refined meshes were used to ensure that the numerical results converge. The contact between the rubber indenter and the glass expands from an initial cone tip to a conical region as the indentation load increases. The finite sliding, hard contact model in ABAQUS (7) was used, to allow for the possibility of sliding between contact surfaces without interpenetration. The normal and shear stress were continuous within the contact process zone. The friction at the contact interface was also accounted for, but it had negligible effect on the indentation load-displacement: the difference between frictionless contact and contact with a large friction coefficient was less than 0.2%. The results of the indentation load vs. displacement (Fig. S7*A*) indicate excellent agreement between FEM and experiments. This outcome validates the use of FEM for a soft indenter in contact with a hard material.

The same FEM techniques were used to model the experimental configuration in the main text. The pyramid microtips, which had the maximum height 10.6 mm, tip radius 100 nm and cone angle 90 degrees between two opposite edges, respectively, was used in the experiments. The Poisson's ratio of microtip is 0.48. Silicon served as the contacting substrate. The element size was ~1.5 nm, which is 70 times smaller than the indenter tip radius, and 7,000 times smaller than the maximum height of microtip. Fig. S7*B* shows the resulting force vs. displacement curve on each microtip, and a comparison to the contact mechanics model (with cone angle 90°) (5) specified in Eqs. **S2** and **S3**, in which P and δ represent the indentation load and displacement, respectively. The numerical and analytical results agree well at small displacements, but begin to deviate as the displacement increases beyond a couple of microns. The present use of the contact mechanics model (5) involves the determination of contact area in the limit of extremely small displacements, associated with zero imposed compressive load. The results in Fig. S7 indicate that the model (5) is applicable in this regime.

A more direct validation of the contact mechanics model (5) is to use FEM to determine the contact radius for the experimental system. To accomplish this goal, we compressed the microtips into contact with the silicon, and then released the load completely, which delaminates the microtip/platelet interface, as simulated by the Cohesive Behavior Model in ABAQUS (7), with a work of adhesion $\gamma = 155$ mJ/m^2, which is consistent with the value reported in the main text. FEM gives a contact radius of 732 nm, which is slightly larger than 680 nm obtained from Eq. **2** based on the contact mechanics model (5). Both values, however, agree, to within experimental uncertainties (~100 nm), with that determined from analysis of SEM images (i.e., 750 nm). Fig. 2*C* (bottom right frame) shows the deformed FEM mesh of final contact (in this zero compressive load regime).

Minimum Height of Microtips. Similar to (8), the minimum height corresponds to the critical state of vanishing preload at which the elastic energy in the stamp due to the collapse of the post equals the adhesion energy between the stamp and platelet. The latter equals the product of work of adhesion γ and contact area, while the former can be obtained using an approach based on fracture mechanics (8), which accounts for the finite geometry of the stamp, such as the stamp width w_{stamp} and contact radius R_{contact} between the microtips and platelet. The contact area is determined analytically by minimizing the total potential energy, which equals the elastic energy in the stamp subtracted by the adhesion energy. The minimum height of microtips is then obtained analytically as

$$h_{\min} = \sqrt{\frac{w_{\text{stamp}}\gamma}{\bar{E}}\left[3.04\ln\left(\frac{w_{\text{stamp}}}{R_{\text{contact}}}\right) - 4.44\right]}, \qquad \textbf{[S8]}$$

where the factors 3.04 and 4.44 result from the stress intensity factor for finite geometry in fracture mechanics. The substitution of the asymptote in Eq. **2** for R_{contact} leads to the analytical expression in Eq. **3**.

Fig. S5*B* shows the minimum height of microtips, normalized by post width w_{stamp}, increases with the work of adhesion γ but decreases with the plane-strain modulus of the stamp. The minimum height for the material properties and post width in experiments is also shown. The experimental data for delamination (above the curve) and collapse (on or below the curve) agree well with the model.

Analysis of Stamp Collapse Process. For the microtip height larger than $h_{\min}$ in Eq. **3**, the process of stamp collapse consists of four stages as the preload P increases; (*i*) microtip contact, during which only microtips contact the platelet; (*ii*) post collapse, which corresponds to a sudden increase of contact area between the post and platelet; (*iii*) post contact, during which the contact area remains the same as the preload increases; and (*iv*) zipping of interface, which corresponds to the increase of contact area with the preload.

i. microtip contact: The deformation in the microtips and post is studied by linear elasticity, where the microtips are subject to uniaxial compression, and the post is subject to the preload and reaction forces from the microtips.
ii. post collapse: The analysis is similar to that for the minimum height, except that the total potential energy includes the external work of the preload. Analytical model gives the following three equations to determine the ratio c_{collapse} of contact area to stamp area at collapse, the corresponding critical load P_{collapse}, and the compressed height h_{collapse} of microtips at collapse,

$$\frac{1}{F_1(b)}\left(\frac{h_{\text{collapse}}}{w_{\text{stamp}}}\right)^2 \frac{K\left(\frac{c_{\text{collapse}}}{b}\right)}{K\left[\sqrt{1-\left(\frac{c_{\text{collapse}}}{b}\right)^2}\right]} - \frac{h_{\text{collapse}}}{w_{\text{stamp}}}\frac{P_{\text{collapse}}}{w_{\text{stamp}}^2\bar{E}}\left[c_{\text{collapse}}\right.$$
$$\left.+\left(\sqrt{2bc_{\text{collapse}}+2c_{\text{collapse}}^2}-2c_{\text{collapse}}\right)F_2(b-c_{\text{collapse}})\right]$$
$$+\frac{3h_{\text{microtip}}}{4w_{\text{stamp}}}(1-b)\left(\ln\frac{h_{\text{collapse}}}{h_{\text{microtip}}}\right)^2 - \frac{4h_{\text{microtip}}}{3w_{\text{stamp}}}\frac{1}{1-b}\left(\frac{P_{\text{collapse}}}{w_{\text{stamp}}^2\bar{E}}\right)^2$$
$$-\frac{2\gamma}{w_{\text{stamp}}\bar{E}}c_{\text{collapse}} = 0, \qquad \textbf{[S9]}$$

$$\frac{1}{F_1(b)}\left(\frac{h_{\text{collapse}}}{w_{\text{stamp}}}\right)^2 \frac{d}{dc}\left\{\frac{K(c/b)}{K[\sqrt{1-(c/b)^2}]}\right\}\Bigg|_{c=c_{\text{collapse}}} - \frac{h_{\text{collapse}}}{w_{\text{stamp}}}\frac{P_{\text{collapse}}}{w_{\text{stamp}}^2\bar{E}}$$
$$\times\left[1+\left(\frac{b+2c_{\text{collapse}}}{\sqrt{2bc_{\text{collapse}}+2c_{\text{collapse}}^2}}-2\right)F_2(b-c_{\text{collapse}})\right.$$
$$\left.-\left(\sqrt{2bc_{\text{collapse}}+2c_{\text{collapse}}^2}-2c_{\text{collapse}}\right)F_2'(b-c_{\text{collapse}})\right]$$
$$-\frac{2\gamma}{w_{\text{stamp}}\bar{E}} = 0, \qquad \textbf{[S10]}$$

$$\frac{1}{F_1(b)}\frac{h_{\text{collapse}}^2}{w_{\text{stamp}}h_{\text{microtip}}}\frac{K(\frac{c_{\text{collapse}}}{b})}{K[\sqrt{1-(\frac{c_{\text{collapse}}}{b})^2}]}+\frac{3(1-b)}{4}\ln\frac{h_{\text{collapse}}}{h_{\text{microtip}}}$$
$$-\frac{h_{\text{collapse}}}{h_{\text{microtip}}}\frac{P_{\text{collapse}}}{w_{\text{stamp}}^2\bar{E}}[F_2(b-c_{\text{collapse}})(\sqrt{2bc_{\text{collapse}}+2c_{\text{collapse}}^2}$$
$$-2c_{\text{collapse}})-1+c_{\text{collapse}}]=0, \quad \textbf{[S11]}$$

where $b=1-\frac{4w_{\text{microtip}}^2}{3w_{\text{stamp}}^2}$, $K(k)=\int_0^{\pi/2}\frac{d\varphi}{\sqrt{1-k^2\sin^2\varphi}}$ is the elliptical function of the first kind, $F_1(k)=-0.417-1.07\ln(1-k)$, and $F_2(k)=(1-0.25k+0.093k^2-0.005k^3)/\sqrt{1-0.5k}$.

iii. post contact: The contact area is the same as that in (*ii*), but the energy release rate at the boundary of contact decreases as the preload increases. The compressed height h' of microtips decreases with the increase of preload, and is given by

$$\frac{1}{F_1(b)}\frac{h'^2}{w_{\text{stamp}}h_{\text{microtip}}}\frac{K(\frac{c_{\text{collapse}}}{b})}{K[\sqrt{1-(\frac{c_{\text{collapse}}}{b})^2}]}+\frac{3(1-b)}{4}\ln\frac{h'}{h_{\text{microtip}}}$$
$$-\frac{h'}{h_{\text{microtip}}}\frac{P}{w_{\text{stamp}}^2\bar{E}}[F_2(b-c_{\text{collapse}})(\sqrt{2bc_{\text{collapse}}+2c_{\text{collapse}}^2}$$
$$-2c_{\text{collapse}})-1+c_{\text{collapse}}]=0. \quad \textbf{[S12]}$$

iv. zipping of interface: The energy release rate at the boundary of contact reaches and remains at zero, and the contact area increases with the preload. The ratio c of contact area to stamp area increases with the preload, while the opposite holds for the compressed height h' of microtips, and they are given by

$$\frac{1}{F_1(b)}\frac{h'^2}{w_{\text{stamp}}h_{\text{microtip}}}\frac{K(\frac{c}{b})}{K[\sqrt{1-(\frac{c}{b})^2}]}+\frac{3(1-b)}{4}\ln\frac{h'}{h_{\text{microtip}}}$$
$$-\frac{h'}{h_{\text{microtip}}}\frac{P}{w_{\text{stamp}}^2\bar{E}}[F_2(b-c)(\sqrt{2bc+2c^2}-2c)-1+c]=0, \quad \textbf{[S13]}$$

$$h'=F_1(b)\frac{P}{w_{\text{stamp}}\bar{E}}\left(1-\frac{c}{b}\right)\sqrt{\frac{c}{2}(b+c)}K\left[\sqrt{1-\left(\frac{c}{b}\right)^2}\right]F_2(b-c). \quad \textbf{[S14]}$$

This analysis gives the following slope change in the preload-distance curve (Fig. 3*A*), maximum height of microtips, and restoring force in microtips.

Slope Change in the Preload-Distance Curve. The distance in Fig. 3*A* before post collapse consists of the (compressive) displacements in microtips and in the post. The microtips are subject to uniaxial compression, while the post is modeled as a semiinfinite solid subject to remote compression and forces from the microtips on the surface. The ratio of preload to this distance gives the slope k_{microtip}

$$\frac{1}{k_{\text{microtip}}}=\frac{1}{w_{\text{microtip}}E}\left[\frac{3h_{\text{microtip}}}{4w_{\text{microtip}}}+\frac{1}{\pi}\left(\frac{w_{\text{microtip}}}{w_{\text{stamp}}}-\frac{2w_{\text{microtip}}^3}{w_{\text{stamp}}^3}\right)\ln\left(\frac{w_{\text{stamp}}^2}{2w_{\text{microtip}}^2}-1\right)\right]+\frac{h_{\text{stamp}}}{w_{\text{stamp}}^2E}, \quad \textbf{[S15]}$$

where h_{stamp} is the effective height of the stamp (Fig. S1*A*).

The change of distance in Fig. 3*A* after post collapse also consists of contributions from the microtips and from the post, but the former becomes negligible as compared to the latter. The ratio of preload increment to distance increment gives the slope k_{post}

$$\frac{1}{k_{\text{post}}}=\frac{h_{\text{stamp}}}{w_{\text{stamp}}^2E}. \quad \textbf{[S16]}$$

Eqs. **S15** and **S16** lead to Eq. **5**.

Restoring Force in Microtips. The restoring force microtips is given by

$$F=P[(\sqrt{2bc+2c^2}-2c)F_2(b-c)-1+c]-\frac{w_{\text{stamp}}\bar{E}}{F_1(b)}\frac{K(\frac{c}{b})}{K(\sqrt{1-\frac{c^2}{b^2}})}h', \quad \textbf{[S17]}$$

where c and h' are determined from Eqs. **S9** to **S14** for stages (*ii*)–(*iv*).

Maximum Height of Microtips. The maximum height of microtips is determined by equating the energy release rate to the work of adhesion, which gives the following relation to determine c

$$\frac{\pi P^2}{4w_{\text{stamp}}^3\bar{E}}(b-c)[F_2(b-c)]^2=\gamma. \quad \textbf{[S18]}$$

Eq. **S14** then gives explicitly h'. The maximum height of microtips, $h_{\max}$, is then obtained from Eq. **S13** by replacing h_{microtip} with $h_{\max}$.

Fig. S5*C* shows the maximum height of microtips, normalized by post width w_{stamp}, increases with the preload as well as the work of adhesion γ but decreases with the plane-strain modulus of the stamp. The maximum height for the material properties and post width in experiments is also shown. The experimental data for retrieval (below the curve) and failure (above the curve) agree well with the model.

Viscoelastic Analysis. For operation in retrieval mode, the PDMS stamp is retracted sufficiently quickly to ensure that the platelet/substrate interface fractures, but the stamp/platelet interface does not, due to effects of viscoelastic behavior in the PDMS. The creep compliance of PDMS, is an important material property that governs this process. This quantity, as measured by Xu et al. (9), can be represented by a piece-wise relation

$$\frac{C(t)}{C(\infty)}=\begin{cases}0.198\times[6.14+\log(t)] & 0.0001<t<0.08\\ 1 & 0.08<t\end{cases}, \quad \textbf{[S19]}$$

which is a nondecreasing function of time t (unit: second). The viscoelastic energy release rate G is related to the stress intensity factor $K(t)$ via the creep compliance by (10)

$$G=\frac{1}{2\bar{E}}\frac{C(t)}{C(\infty)}K^2(t), \quad \textbf{[S20]}$$

where $\bar{E}$ is the plane-strain modulus of PDMS, and the factor $1/2$ accounts for the elastic mismatch between PDMS and silicon (8). The stress intensity factor $K(t)$ is given by

$$K_I=\frac{\bar{E}h''}{F_1(b)}\sqrt{\frac{\pi}{2w_{\text{stamp}}c[1-(\frac{c}{b})^2]}}\frac{1}{K[\sqrt{1-(\frac{c}{b})^2}]}$$
$$+\frac{P''}{2w_{\text{stamp}}}\sqrt{\frac{\pi(b-c)}{w_{\text{stamp}}}}F_2(b-c), \quad \textbf{[S21]}$$

where w_{stamp} is the stamp width, b and functions F_1, F_2, and K are defined after Eq. **S11**, c is solved from Eqs. **S13** and **S14**, P'' is the pull-off force, and the microtip height h'' is related to P'' by

$$\frac{1}{F_1(b)}\frac{h''^2}{w_{\text{stamp}}h_{\text{microtip}}}\frac{K(\frac{c}{b})}{K[\sqrt{1-(\frac{c}{b})^2}]}+\frac{3(1-b)}{4}\ln\frac{h''}{h_{\text{microtip}}}$$
$$+\frac{h''}{h_{\text{microtip}}}\frac{P''}{w_{\text{stamp}}^2\tilde{E}}[F_2(b-c)(\sqrt{2bc+2c^2}-2c)-1+c]=0, \quad \textbf{[S22]}$$

which is identical to Eq. **S13** except that P and h' are replaced by $-P''$ and h'', respectively.

The pull-off force is related to the pulling speed v_{pulling} and time t by

$$P''=w_{\text{stamp}}E(v_{\text{pulling}}t-L_{\text{compression}}), \quad \textbf{[S23]}$$

after the compression force P is relaxed, where $L_{\text{compression}}$ is the compressed distance of the stamp due to P, and $L_{\text{compression}} = 20$ μm from Fig. 3*A*.

The stamp/platelet interface will not delaminate if the viscoelastic energy release rate remains smaller than the work of adhesion γ, i.e.,

$$G<\gamma \quad \textbf{[S24]}$$

For the material properties given in the main text, the creep compliance in Eq. **S19**, and pulling speed $v_{\text{pulling}} = 460$ μm/s, the above inequality gives a critical time of 0.052 s for the stamp/platelet interface starting to debond. The pull-off force is then obtained from Eq. **S23**.

1. Hourdakis E, Simonds BJ, Zimmerman NM (2006) Submicron gap capacitor for measurement of breakdown voltage in air. *Rev Sci Instrum* 77:034702-1–034702-4.
2. Cao Q, et al. (2007) Gate capacitance coupling of single-walled carbon nanotube thin-film transistors. *Appl Phys Lett* 90:023516-1–023516-3.
3. Zhou X, Park JY, Huang S, Liu J, McEuen PL (2005) Band structure, phonon scattering, and the performance limit of single-walled carbon nanotube transistors. *Phys Rev Lett* 95:146805-1–146805-4.
4. Cao Q, Rogers JA (2009) Ultrathin films of single-walled carbon nanotubes for electronics and sensors: a review of fundamental and applied aspects. *Adv Mater* 21:29–53.
5. Maugis D (1995) Extension of the Johnson-Kendall-Roberts Theory of the elastic contact of spheres to large contact radii. *Langmuir* 11:679–682.
6. Lim YY, Chaudhri MM (2003) Experimental investigations of the normal loading of elastic spherical and conical indenters on to elastic flats. *Philos Mag* 83:3427–3462.
7. Dassault Systèmes (2009) *Abaqus analysis user's manual v.6.9*. (Dassault Systèmes Simulia Corp., Rhode Island).
8. Huang Y, et al. (2005) Stamp collapse in soft lithography. *Langmuir* 21:8058–8068.
9. Xu Z, et al. (2008) Broadband measurement of rate-dependent viscoelasticity at nanoscale using scanning probe microscope: Poly(dimethylsiloxane) example. *Appl Phys Lett* 93:133103.
10. Schapery RA (1975) A theory of crack initiation and growth in viscoelastic media II. Approximate methods of analysis. *Int J Fracture* 11:369–388.

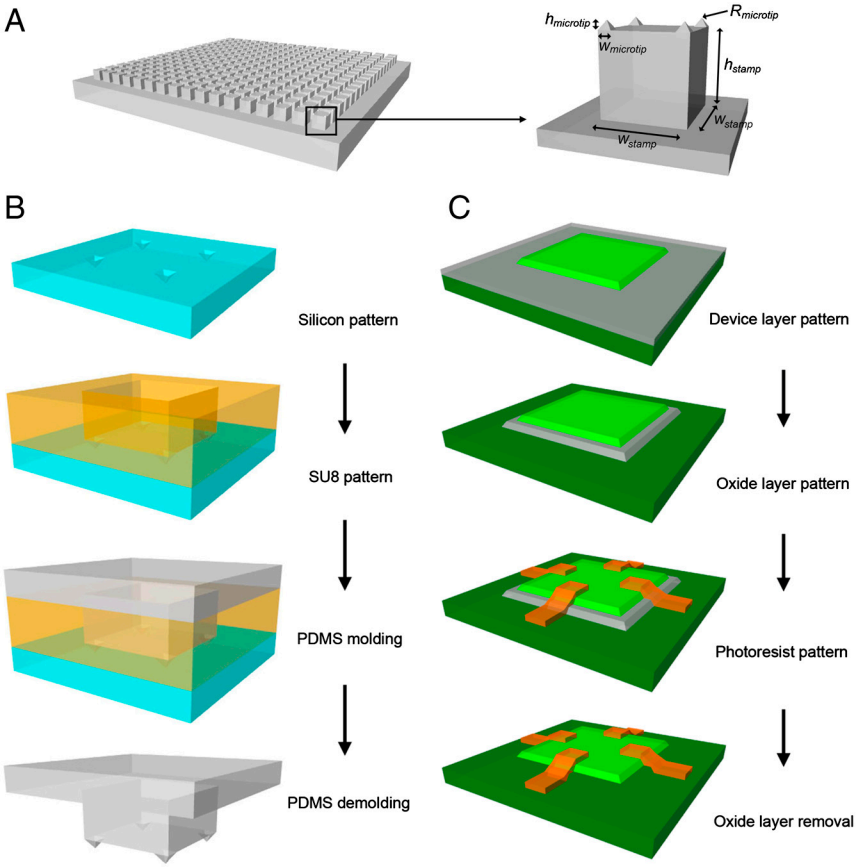

Fig. S1. (*A*) Elastomeric, microtip adhesive surface consisting of four features of pyramidal relief on the surfaces of square posts in a square array. (*B*) Schematic illustration of the process for making microtip stamps of PDMS by casting and curing against a photolithographically defined pattern of SU8 on an anisotropically (KOH) etched silicon (100) wafer. (*C*) Schematic illustration of the process for fabricating silicon platelets in printable configurations, starting with silicon-on-insulator (SOI) wafers with 3 μm or 260 nm thick top Si layers.

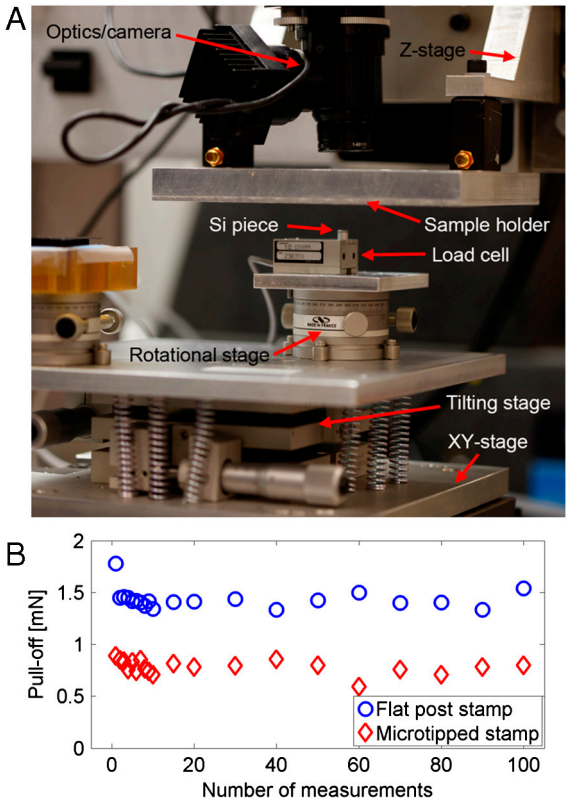

Fig. S2. (*A*) Picture of a custom adhesion testing setup design to measure pull-off forces with elastomeric, microtip stamps. (*B*) Pull-off force data of a stamp with four-tipped layout and a corresponding flat surface measured repeatedly with 200 μm/s retraction speed and 2 mN preload constantly up to 100 times.

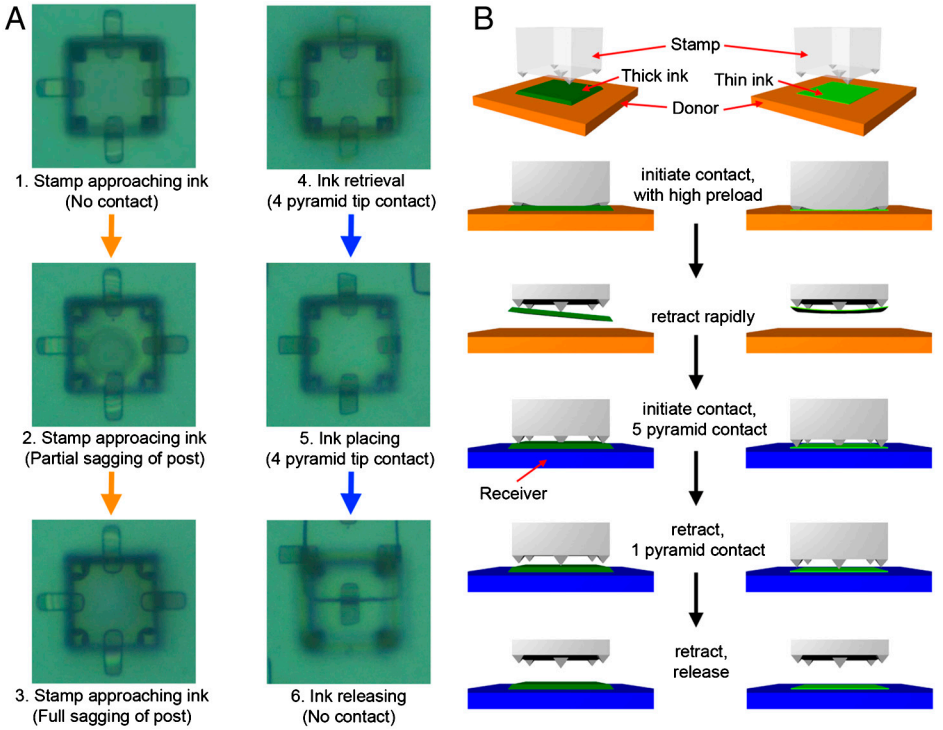

Fig. S3. (*A*) Optical microscope top view images, collected by viewing through a transparent microtip stamp, during various stages of the printing. (*B*) Schematic illustration of the process for transfer printing with a microtip stamp that has a five-tipped design. The largest microtip, located at center, is the only point of contact between the stamp and the ink at the final stage of the transfer process.

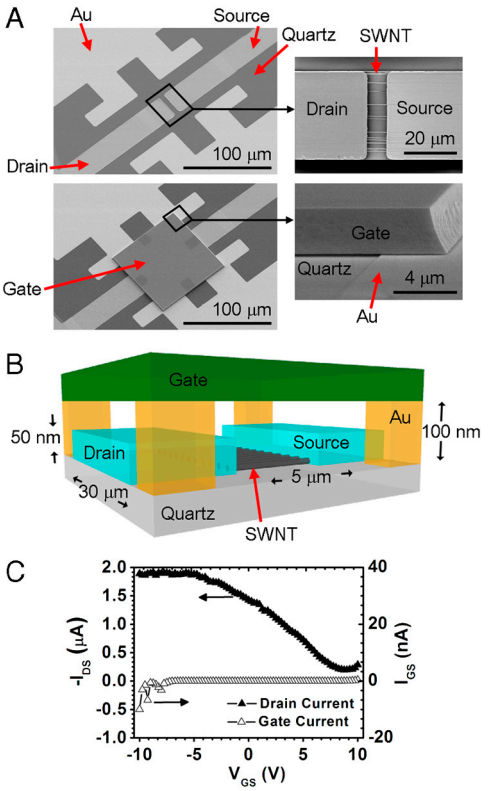

Fig. S4. (*A*) SEM images of carbon nanotube field effect transistor (CNFET) with 100 nm thick air gap dielectric fabricated using transfer printing a heavily doped ($\rho = 0.0014\ \Omega$cm) silicon platelet (3 μm thick; 100 × 100 μm). The right frames provide the magnified view of single walled carbon nanotubes (SWNTs) under the silicon platelet and 100 nm air gap between a gate and a quartz substrate in the left frames. (*B*) Schematic illustration of the CNFET with dimensions. (*C*) Transfer characteristics for the CNFET.

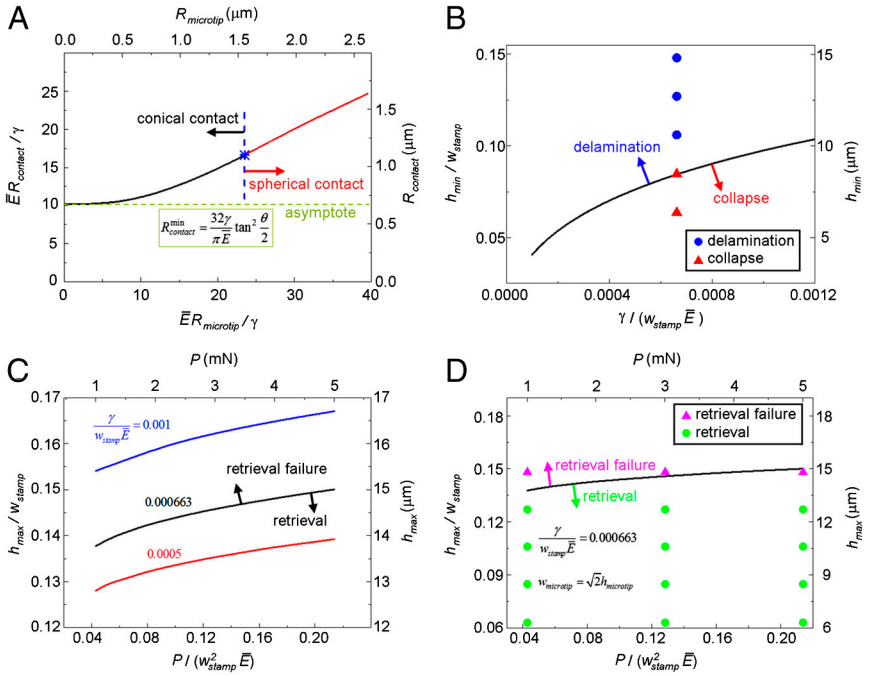

Fig. S5. (*A*) The contact radius (at zero preload) between the microtips and platelet vs. the microtip radius of curvature for the microtip cone angle $\theta = 90°$. The asymptote for vanishing microtip radius gives minimal contact radius. (*B*) The minimum height of microtips vs. the work of adhesion (normalized by the post width and plane-strain modulus of the stamp) for $\theta = 90°$, together with the experimental data for delamination and collapse. (*C*) The maximum height of microtips vs. the preload for several values of work of adhesion. (*D*) The maximum height of microtips vs. the preload, together with the experimental data for retrieval and failure.

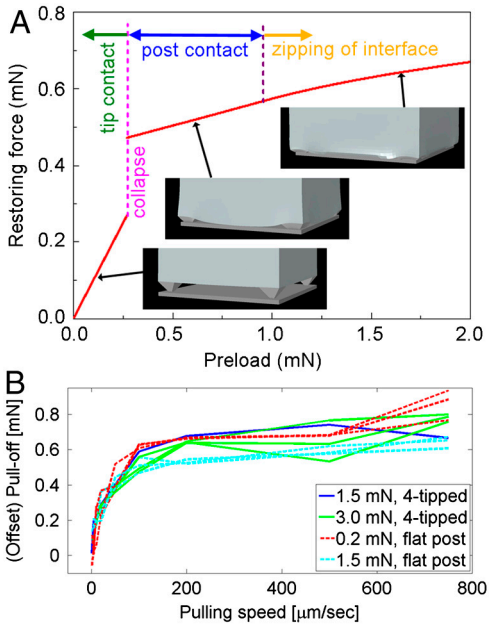

Fig. S6. (*A*) Restoring force associated with compression of microtips on the surface of an elastomer as a function of preload, during loading with corresponding images of finite element modeling results. (*B*) Master plot of force required to separate an elastomer surface from a flat substrate, as a function of retraction speed for different preload cases from Fig. 3*C*, *D*. The data include the cases of elastomeric posts that terminate in flat surfaces and in sets of four microtips, scaled to account for the mechanics of the microtips, according to theoretical modeling.

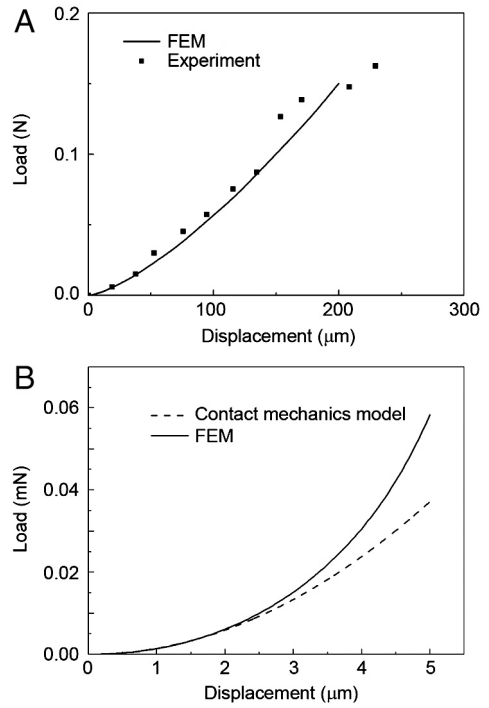

Fig. S7. (*A*) Load-displacement comparison between FEM results and experimental data for the case of the system of Lim and Chaudhri. (*B*) Load-displacement comparison between FEM results and contact mechanics model for a PDMS microtip pressed against a silicon substrate.